PAPER

Check for updates

Reduced graphene oxide-mediated synthesis of Mn_3O_4 nanomaterials for an asymmetric supercapacitor cell

Mingyan Gao,[a] Xiaofeng Wu,[b] Haifang Qiu,[a] Qingfan Zhang,[a] Keke Huang,[b] Shouhua Feng, [ID][b] Ying Yang, [ID][a] Tingting Wang, [ID][a] Bo Zhao [ID] *[ab] and Zhelin Liu [ID] *[a]

Herein, Mn_3O_4/reduced graphene oxide composites are prepared *via* a facile solution-phase method for supercapacitor application. Transmission electron microscopy results reveal the uniform distribution of Mn_3O_4 nanoparticles on graphene layers. The morphology of the Mn_3O_4 nanomaterial is changed by introducing the reduced graphene oxide during the preparation process. An asymmetric supercapacitor cell based on the Mn_3O_4/reduced graphene oxide composite with the weight ratio of 1 : 1 exhibits relatively superior charge storage properties with higher specific capacitance and larger energy density compared with those of pure reduced graphene oxide or Mn_3O_4. More importantly, the long-term stability of the composite with more than 90.3% capacitance retention after 10 000 cycles can ensure that the product is widely applied in energy storage devices.

1.   Introduction

The exhaustion of fossil energy and the deterioration of the environment are becoming increasingly serious for human beings. Therefore environmentally friendly, flexible and lightweight novel energy storage devices such as supercapacitors (SCs), also called electrochemical capacitors (ECs), have attracted urgent attention in recent years. Their high power density, relatively low weight, exceptional long-term stability and quick response to potential changes[1,2] significantly remedies some limitations of conventional batteries.[3] However, despite such excellent properties, the energy density of most commercial ECs is lower than that of lithium ion batteries,[4] and pseudocapacitors usually have short cyclic lifetimes[5] which make it a challenge to improve the performance of SCs.

In the light of the active electrode materials applied and the charge storage mechanism occurring, the SCs can be simply classified as electrical double layer capacitors (EDLCs),[6,7] pseudocapacitors[8,9] or hybrid capacitors.[10] Over the past decades, research into electrode materials for improving the energy density of SCs has never ceased. The charge storage mechanism of EDLCs is mainly based on the accumulation of charges at the interfaces between the high-surface-area electrodes and the

electrolyte ions, and the corresponding capacitance is closely related to the surface area and the porous structure of the electrode materials.[11,12] Many different forms of carbon-based active materials, such as activated carbon (AC),[13–15] graphene nanosheets,[16] and carbon nanotubes[17] have been widely applied in EDLCs. Among all these carbonaceous materials, the sp2-hybridized graphene is a promising active material for EDLCs, due to its unique two-dimensional nanostructure, very high theoretical surface area, excellent electrical conductivity, and good mechanical properties, in addition to its environmentally friendly nature.[18] However, these apparent properties of graphene cannot significantly promote the specific capacitance of ECs. Thus, integrating graphene nanosheets with other pseudocapacitive materials, including some transition-metal oxides or conducting polymers, to form a hybrid electrode should be a possible way of fully realizing the potential application of graphene.

In recent years, attempts have been made to explore inexpensive transition-metal oxide nanomaterials such as manganese oxide,[19–21] cobalt oxide,[22,23] nickel oxide,[24] cobalt hydroxide,[25] and nickel hydroxide[26] due to their potential to offer much higher energy densities and specific capacitances than typical carbon-based EDLCs and conducting polymers.[27] Among them, Mn_3O_4 nanomaterials have been reported as promising electrode materials for supercapacitor application[28] owing to the high abundance of the Mn element, environmental benignity, low cost, satisfactory energy storage performance, and relatively wide work potential window of these nanomaterials in aqueous solution.[29] As a result, much effort has been dedicated to the combining of graphene nanosheets with

[a]Key Laboratory of Applied Chemistry and Nanotechnology at Universities of Jilin Province, Department of Chemistry & Environmental Engineering, Changchun University of Science and Technology, Changchun, Jilin 130022, P. R. China. E-mail: b.zhao@live.cn; zl.liu@live.cn; Fax: +86-431-85583447; Tel: +86-431-85583447

[b]State Key Laboratory of Inorganic Synthesis and Preparative Chemistry, College of Chemistry, Jilin University, Changchun, Jilin 130012, P. R. China

Mn_3O_4 for the sake of obtaining superior capacitive performance.[30,31] Generally, graphene–Mn_3O_4 composites are prepared by using manganese sources as precursors and ultra-thin flexible graphene oxide (GO) or reduced graphene oxide (rGO) sheets as a highly conductive substrate.[32] GO is usually fabricated by the Hummers' method,[33] which leads to numerous functional groups on its basal planes and edges, such as hydroxyl, carboxyl, and aldehyde groups.[34] It is worth noting that the existence of these functional groups is beneficial to the firm attachment of Mn_3O_4 nanoparticles[35] and induces superior hydrophilicity towards electrolyte solutions.[36]

In order to realize the efficient practical application of an Mn_3O_4/rGO (MG) nanocomposite, advanced supercapacitors with high cell voltages must be developed to elevate the energy density without sacrificing the power density or cycling life. An asymmetric supercapacitor cell fabricated by combining a positive electrode (or battery-like faradic electrode) and a negative electrode (or capacitive electrode) can combine the virtues of batteries (large energy density) and supercapacitors (high power density and long-term stability).[28] Based on the above merits, the assembly of an asymmetric supercapacitor cell is utilized as a novel and practical method in our electrochemical measurements. Hitherto, it has been a challenge to produce pure Mn_3O_4 nanostructures due to the multiple valences of Mn ions, and continuous attempts have been made to distribute Mn_3O_4 nanoparticles with high uniformity and fine granularity onto GO or rGO sheets.[36]

In this work, a facile solution-phase method is presented for attaching zero-dimensional (0D) Mn_3O_4 nanoparticles on rGO nanosheets to form a MG hybrid electrode material. The MG hybrid is afterwards freeze-dried, obtaining a loosely stacked structure. It is interesting that when rGO is absent, the morphology of the Mn_3O_4 nanomaterial changes to that of a one-dimensional (1D) structure in the investigated system. This peculiar phenomenon is of great importance to the study of the crystal growth mechanism on the graphene surface and the interface between the two components. The electrochemical characteristics of the as-synthesized MG nanocomposite are further investigated by assembling asymmetric supercapacitor cells with two electrodes.

2. Experimental

2.1 Materials

All chemicals used throughout the study were of at least analytical grade and were used as received, without purification. Ultrapure water with a resistivity no less than 18.2 MΩ cm was used.

2.2 Synthesis of graphene oxide

Graphene oxide (GO) was prepared by a modified Hummers' method from natural graphite powder.[33] Firstly, 2 g $K_2S_2O_8$ and 2 g P_2O_5 were put into 15 mL concentrated H_2SO_4 and the mixture was heated to 80 °C. Then, 1 g graphite powder was added until the solids were completely dissolved, and the mixture was stirred for 8 h at 80 °C. After that, the mixture was

transferred into 1.8 L of water and left still for at least 12 h. Then, the mixture was washed with 2.5 L of water and dried at room temperature for 24 h. The product was put into 150 mL concentrated H_2SO_4 in an ice-water bath and then 10 g $KMnO_4$ was slowly added with stirring. After the absolute dissolution of the $KMnO_4$, the mixture was stirred for 2 h at 35 °C. The resulting solution was then gradually dispersed into 4 L of cooled water with stirring. After 5 min of stirring, the mixing speed was raised and 30 mL of 30% H_2O_2 was quickly added to the solution. The colour of the solution changed sharply from purple to brilliant yellow, generating a large number of bubbles. The mixture was filtered and then washed with 400 mL 1 : 10 HCl to water (v/v). The resulting product was subsequently washed with 4 L of water and finally dried by vacuum freeze-drying.

2.3 Synthesis of rGO

For the synthesis of rGO,[37] 0.15 g GO was added to 300 mL of *N,N*-dimethylformamide (DMF), and the mixed solution was refluxed under vigorous stirring at 160 °C for 3 h. After cooling to room temperature, it was sonicated for 30 min to obtain an rGO-DMF dispersion (0.5 mg mL^{-1}). Then the as-prepared rGO-DMF dispersion was filtered, washed with water and dried by vacuum freeze-drying to obtain rGO.

2.4 Synthesis of MG nanocomposites

In this work, MG nanocomposites with different weight ratios of Mn_3O_4 to rGO (1 : 9, 1 : 3, 1 : 1) were prepared, named as MG-10, MG-25 and MG-50, respectively. The synthesis process of MG-25 is described as an example. Firstly, 17.2 mg $KMnO_4$ was dissolved in 50 mL of rGO-DMF dispersion (0.5 mg mL^{-1}). Then the mixture was refluxed at 160 °C for 3 h with stirring. After 3 h of reaction, the as-prepared dispersion was cooled to room temperature and then filtered and washed with water. The product was finally dried by means of vacuum freeze-drying. In order to investigate the effects of the reduction temperature and reaction time, composites with the weight ratio of 1 : 1 were prepared by reduction at 160 °C for 1 h, 2 h and 3 h, as well as at the temperatures of 100 °C, 120 °C and 140 °C for 3 h.

2.5 Synthesis of pure Mn_3O_4 nanomaterials

The process to synthesize the pure Mn_3O_4 nanomaterial was similar to that for the preparation of MG nanocomposites. Briefly, 20 mg $KMnO_4$ was dissolved in 50 mL DMF and refluxed with stirring at 160 °C for 3 h. The resulting product was then filtered, washed with water and dried under vacuum.

2.6 Structure and morphology characterization

X-ray diffraction (XRD) analyses were carried out on a D/max 2550 V/PC X-ray diffractometer. The morphology of the MG composites was characterized by transmission electron microscopy (TEM) and high-resolution transmission electron microscopy (HRTEM) on a Tecnai G2 S-Twin F20 transmission electron microscope. X-ray photoelectron spectroscopy (XPS) was performed on an ESCALAB-MKII spectrometer (United

Kingdom). Raman spectra were obtained with a Renishaw 2000 Raman spectrometer (United Kingdom).

2.7 Electrochemical measurements

In this study, the assembled asymmetric supercapacitor cells designated as MG-10//GO, MG-25//GO, MG-50//GO, rGO//GO and Mn_3O_4//GO were fabricated with two electrodes using 1 M Na_2SO_4 aqueous solution as the electrolyte. The positive and negative electrodes were prepared as follows. For the positive electrode, active powder, acetylene black, and poly-(vinylidenefluoride) (PVDF) were mixed using N-methyl-2-pyrrolidone (NMP) as the solvent in a weight ratio of 80 : 15 : 5. For the negative electrode, GO powder was used as the active powder, and the weight ratio was 80 : 10 : 10. After sufficient grinding, the paste was coated onto a round nickel foam (1.5 cm^2), which was then allowed to dry at 110 °C for 12 h. The dried foam was then pressed at 10 MPa. The electrochemical measurements, including cyclic voltammetry (CV), galvanostatic charge–discharge (GCD) testing as well as electrochemical impedance spectroscopy (EIS), were all performed on a CHI 660E electrochemical analyzer (Chenhua Co., Shanghai, China). EIS was measured in the frequency range of 100 kHz to 1 Hz and at the potential amplitude of 5 mV.

The specific capacitance C_s (F g^{-1}) was calculated from the GCD curve based on the following equation:

$$C_s = I\Delta t/(m\Delta V) \quad (1)$$

where I (A) is the discharge current, Δt (s) is the discharge time, m (g) is the mass of active material, and ΔV (V) is the discharge potential range.

The energy density E (W h kg^{-1}) and power density P (W kg^{-1}) were calculated according to the following equations:

$$E = C_s\Delta V^2/2 \quad (2)$$

$$P = E/\Delta t \quad (3)$$

3. Results and discussion

3.1 Structural characterization

The MG composites were fabricated by a facile solution-phase method followed by freeze-drying. The XRD pattern (Fig. 1a, upper part) of MG-50 prepared at 160 °C shows that the prepared manganese oxide can be indexed to Mn_3O_4 (JCPDS no. 24-0734). Diffraction peaks located at 18.0°, 28.9°, 32.3°, 36.1° and 59.8° correspond to the (101), (112), (103), (211) and (224) crystallographic planes of hausmannite Mn_3O_4, respectively, indicating the successful fabrication of Mn_3O_4 via this approach. It is worth noting that although K$^+$ ions were present in the preparation process, no K-birnessite is observed in the final product. We performed further investigations to ascertain whether or not the product could be acquired at lower temperatures. Thus, products were prepared at 100 °C, 120 °C, and 140 °C while keeping the other conditions identical. As
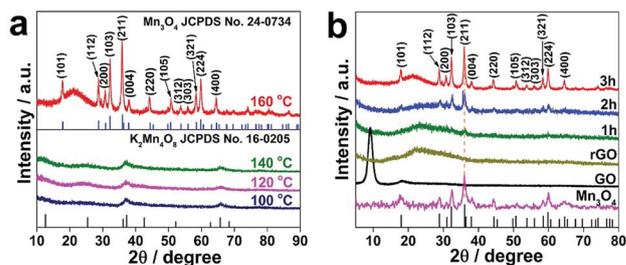

Fig. 1 XRD patterns of reduced products prepared (a) at different temperatures (100 °C, 120 °C, 140 °C and 160 °C) for 3 h and (b) after different durations (1 h, 2 h and 3 h) at 160 °C, compared with rGO, GO and pure Mn_3O_4.

shown in Fig. 1a (lower part), the XRD patterns of the manganese compounds prepared at or below 140 °C can be indexed to $K_2Mn_4O_8$ (JCPDS no. 16-0205), indicating that the lower temperature is not sufficient for heating DMF to produce CO as the reducing agent for efficient reduction of KMnO$_4$. Thus, the reaction temperature of 160 °C was employed during the preparation process to further investigate the reaction time, and the XRD patterns are shown in Fig. 1b. It can be found that peaks ranging from 15.0° to 28.0° ascribed to rGO can be seen for all the samples prepared at different durations, indicating that the products are composites of Mn_3O_4 and rGO. In addition, the relative intensity of the peak corresponding to the (211) plane of Mn_3O_4 gradually increases with the extension of reduction time (as marked with the dotted line), which indicates the high crystallinity of the Mn_3O_4 that was prepared after 3 h. The bottom pattern displayed in Fig. 1b reflects the fact that pure Mn_3O_4 can be obtained under the same reduction condition as that of the MG composites.

TEM was utilized to study the microstructures of the samples prepared in this work. It is clear to see the high-quality thin layers of GO and rGO from Fig. 2a and b, respectively. Fig. 2c, d and e display the MG-10, MG-25 and MG-50 composites with increasing weight ratios of Mn_3O_4 to rGO (1 : 9, 1 : 3, 1 : 1). The
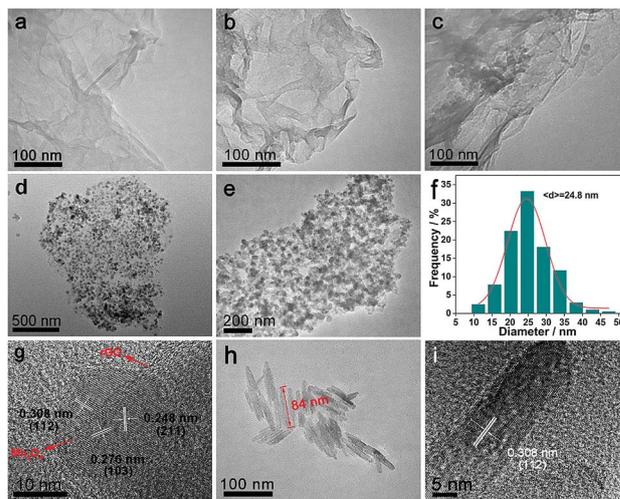

Fig. 2 TEM images of (a) GO, (b) rGO, (c) MG-10, (d) MG-25, (e) MG-50, and (h) pure Mn_3O_4. HRTEM images of (g) MG-50 and (i) pure Mn_3O_4. (f) Corresponding particle size distribution of MG-50.

quantity of Mn_3O_4 nanoparticles on the rGO surface rises obviously with the increase in weight ratio. However, the morphology, as well as the uniform distribution of Mn_3O_4 nanoparticles, is still maintained and no remarkable agglomeration is observed at the different weight ratios. Herein, the MG-50 composite is used as the example in further characterizations. Fig. 2f displays the particle size distribution of MG-50, which was statistically evaluated by measuring the diameter of 100 randomly picked Mn_3O_4 nanoparticles from Fig. 2e. The data shows a normal distribution and an average diameter of the nanoparticles of 24.8 nm. The good dispersion of Mn_3O_4 nanoparticles with relatively uniform diameters on MG-50 is beneficial for creating enough adsorption sites, which may improve the electrochemical performance of the composite.[38] Besides, the TEM image shown in Fig. 2h further reveals the 1D morphology of the Mn_3O_4 nanomaterial obtained without combination with rGO. Thus, it can be seen that the combination of Mn_3O_4 and rGO gives rise to a morphological change of Mn_3O_4 from the 1D structure in the absence of rGO to 0D nanoparticles in the presence of rGO. The morphological change may be the result of the attachment of rGO and Mn_3O_4, which hinders the oriented growth of the Mn_3O_4 crystal. The connection formed between Mn_3O_4 and rGO may be beneficial to the electrochemical behaviour of the resulting composite. More details of the MG-50 composite and bare Mn_3O_4 nanomaterials can be seen in the HRTEM images of Fig. 2g and i, respectively. Both two forms of crystalline Mn_3O_4 particles have a distance between adjacent planes of ca. 0.308 nm, corresponding to the (112) crystal plane, while the (103) and (211) crystal planes of the MG composite can also be identified from the d-spacings of 0.276 nm and 0.248 nm, further suggesting the successful preparation of Mn_3O_4 on the rGO surface.

To investigate the surface elements and valence states of the MG composites, XPS analysis was employed. As shown in Fig. 3a, the main XPS peaks of C 1s, O 1s, Mn $2p_{3/2}$, and Mn $2p_{1/2}$ displayed in the survey spectrum indicate the three primary

elements in the MG composites. Fig. 3b reveals that the C 1s spectrum can be reasonably deconvoluted into four peaks, which are assigned to the following carbonaceous functional groups: C–C (284.6 eV), C–O (286.2 eV), C=O (288.0 eV) and O–C=O (289.0 eV).[39] The C–C peak with high intensity indicates the existence of a stable sp^2-hybridized graphitic structure. The peaks are in good agreement with those reported for rGO,[40] revealing that the graphite structure is maintained well after the composite process. The Mn 2p spectrum exhibits two peaks for Mn $2p_{3/2}$ and Mn $2p_{1/2}$ located at 642.2 eV and 653.8 eV, respectively, with a splitting width of 11.6 eV (Fig. 3c), which is well in line with the value of an earlier reported Mn_3O_4–rGO hybrid material,[41] further confirming the formation of Mn_3O_4. As shown in Fig. 3d, the fitting curves of the O 1s peaks at 529.9 eV, 531.5 eV and 532.4 eV can be attributed to Mn–O–Mn (for anhydrous oxide), Mn–O–H (for hydroxide), and H–O–H (for crystalline water), respectively.[39] According to the O 1s spectrum, the valence state of manganese can be calculated as +2.82,[42,43] which is similar to the theoretical valence state (+2.67) of the manganese element in Mn_3O_4, calculated according to JCPDS no. 24-0734.

Raman spectroscopy was used to provide further structural information on the samples before and after reduction, as shown in Fig. 4. Compared with the GO and rGO spectra, the MG-50 composite has an extra Raman peak, corresponding to hausmannite Mn_3O_4, at approximately 653 cm^{-1} and indicating the existence of both Mn_3O_4 nanoparticles and an rGO layer.[44] The Raman spectra of these three samples all have two broad peaks ascribed to the well-documented D band (at ~1358 cm^{-1}) and G band (at ~1599 cm^{-1}). The D band, caused by the breathing vibrational modes of sp^2-hybridized carbon rings, is related to the structural defects as well as the oxidation process of graphene, and the G band derives from the fundamental vibration mode and the average size of the graphite crystals.[45] The intensity ratio of the D and G bands (I_D/I_G) of the MG composite is similar to that of rGO, consistent with the previous XPS result (Fig. 3b), and indicating that the graphite structure does not undergo a significant change after the assembly process. It is worth noting that the I_D/I_G value of the MG composite is only increased slightly in comparison with that of
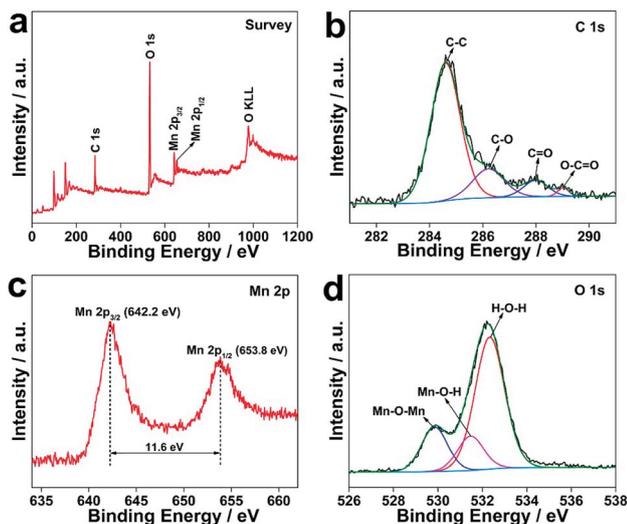

Fig. 3   (a) XPS survey scan, and (b) C 1s, (c) Mn 2p and (d) O 1s spectral regions of the MG-50 composite.
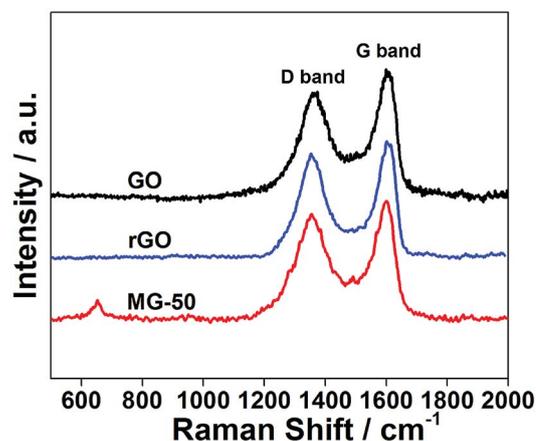

Fig. 4   Raman spectra of GO, rGO and the MG-50 nanocomposite.

GO, and that the intensity of the G band is still higher than that of the D band, demonstrating the remaining low degree of disorder and large sp^2 domains of rGO after the reduction process.

3.2 Electrochemical performance of asymmetric supercapacitor cells

Asymmetric supercapacitor cells were fabricated as devices for studying the capacitive performance for practical applications, using MG composites and GO coated nickel foams as the positive electrodes and negative electrodes, respectively, and 1 M Na_2SO_4 aqueous solution as the electrolyte. Herein, the MG-50//GO supercapacitor cell is used as an example for the electrochemical measurements. Fig. 5a displays the CV curves of the MG-50//GO supercapacitor cell in different potential windows at the scan rate of 50 mV s^{-1}. It can be observed that there is no obvious increment of the anodic current density even at 1.6 V, indicating that the assembled asymmetric supercapacitor cell can be reversibly cycled and is stable in different voltage windows. The GCD curves are constant symmetrical triangular shapes for MG-50//GO in the different potential windows at the current density of 1 A g^{-1} as shown in Fig. 5b, further demonstrating the good capacitive behaviour of the electrode material. Therefore, the extended potential window of 0–1.6 V was selected as the stable operational voltage range for further electrochemical measurements. The CV behaviour of MG-50//GO was further investigated by varying the scan rate from 1 mV s^{-1} to 50 mV s^{-1}. As shown in Fig. 5c, the CV curves of MG-50//GO maintain the rectangle-like shapes despite increasing scan rates, suggesting the ideal electron-transfer kinetics and good rate capability of the asymmetric supercapacitor. Moreover, no obvious redox peak is observed from the CV curves of the composite compared with that of bare Mn_3O_4 (Fig. 5d). This should be ascribed to the presence of rGO that makes the

double layer behaviour stronger than the faradic reaction of Mn_3O_4.[46] We compared the CV curves (Fig. 5d) of rGO//GO, MG-10//GO, MG-25//GO, MG-50//GO, and Mn_3O_4//GO at the same scan rate of 50 mV s^{-1}. In general, the specific capacitance is proportional to the area of the CV curves. In this study, the specific capacitance gradually increases with the rising weight ratio of Mn_3O_4 to rGO, and finally reaches its maximum value when the weight ratio is 1 : 1, which corresponds to the MG-50 composite.

The capacitive performance of the MG-50//GO supercapacitor cell at different current densities was determined through GCD testing as shown in Fig. 6a. All the GCD curves retain an approximately symmetrical shape at different current densities from 0.2 A g^{-1} to 8 A g^{-1} in the potential window of 0–1.6 V, manifesting the high reversibility between the charge and discharge processes.[34] The GCD performances of rGO//GO, MG-50//GO and Mn_3O_4//GO at the current density of 1 A g^{-1} are compared (Fig. 6b), and the specific capacitances of the three samples at different current densities are also calculated (Fig. 6c). According to the calculation results, the MG-50//GO supercapacitor cell can deliver an excellent specific capacitance of 313.7 F g^{-1} at a current density of 0.2 A g^{-1}, remarkably higher than that of the other two materials, which may be attributed to the direct combination of the Mn_3O_4 nanoparticles with the rGO nanosheets and the intimate interactions between the nanolayers, that greatly enhances the charge transfer efficiency between the Mn_3O_4 nanoparticles and the highly conducting graphene network.

The Ragone plots (Fig. 6d) are obtained from GCD tests of the assembled asymmetric supercapacitor cells at different power densities. The MG-50//GO assembled asymmetric supercapacitor cell exhibits a high energy density of 59.6 W h kg^{-1} at a power density of 8752 W kg^{-1}, which is superior to those of Mn_3O_4/graphene asymmetric supercapacitors[5,28,47–49] previously reported, such as the CNTG-40//
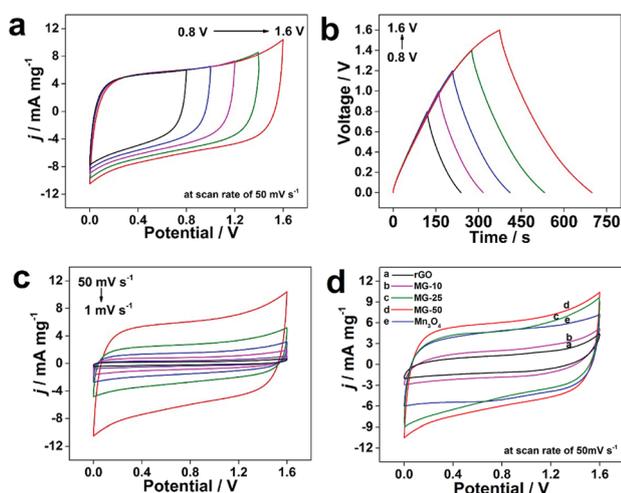
Fig. 5 CV curves of (a) MG-50//GO in different potential windows in 1 M Na_2SO_4 aqueous solution at the scan rate of 50 mV s^{-1}, (c) MG-50//GO at various scan rates and (d) five different supercapacitor cells with different composites at the scan rate of 50 mV s^{-1}. (b) GCD curves of MG-50//GO in different potential windows at the current density of 1 A g^{-1}.
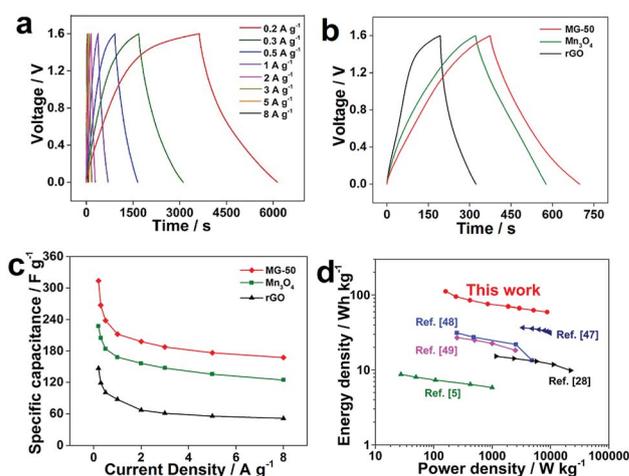
Fig. 6 GCD curves of (a) MG-50//GO at different current densities ranging from 0.2 A g^{-1} to 8 A g^{-1}, and (b) three different supercapacitor cells at a current density of 1 A g^{-1}. (c) Specific capacitances of the three supercapacitor cells at varied current densities. (d) Ragone plots comparing MG-50//GO and the Mn_3O_4/graphene asymmetric supercapacitors as previously reported.

MG-50 all-solid-state symmetric supercapacitor (22.9 W h kg^{-1} at 9.0 kW kg^{-1}),[47] the Mn$_3$O$_4$-GO double-shell hollow sphere asymmetrical supercapacitor (13.5 W h kg^{-1} at 4844 W kg^{-1}),[48] the Mn$_3$O$_4$/RGO-0.35 electrode (18.3 W h kg^{-1} at 2500 W kg^{-1}),[49] the GMn80//N-doped RGO aqueous asymmetric supercapacitor (11.11 W h kg^{-1} at 23.5 kW kg^{-1})[28] and the RCDGO/Mn$_3$O$_4$-86 aqueous symmetrical supercapacitor (5.8 W h kg^{-1} at 1.0 kW kg^{-1}).[5]

The long-term cyclic stability was tested at a high current density of 8 A g^{-1} (Fig. 7a). The capacitance retention of the MG-50//GO assembled asymmetric supercapacitor cell reaches almost 90.3% after repeating the GCD tests for 10 000 cycles and no appreciable degradation is observed, suggesting that the MG-50 composite exhibits excellent stability as an electrode material for supercapacitor application.[11]

EIS was carried out to further study the resistive, capacitive and ion-transport properties of the assembled asymmetric supercapacitor cells. Fig. 7b compares the Nyquist plots of MG-50//GO, Mn$_3$O$_4$//GO and rGO//GO supercapacitor cells with a frequency range between 1 Hz and 100 kHz. A Nyquist plot shows the relation between the imaginary component of the impedance (Z'') against the real component (Z'), where the lower left portion of the curve refers to higher frequencies. The diagonal line in the low frequency region gives the Warburg impendence (W), which corresponds to the ion diffusion at the interface between the active electrode material and electrolyte.[50] The higher tendency of the diagonal line inclining to the imaginary axis in the low frequency region of MG-50//GO indicates the nearly ideal capacitive performance of this cell. The semicircle in the intermediate frequency region reflects the interfacial charge transfer resistance (R_{CT}) and double layer capacitance (C_{DL}).[51] The R_{CT} value for MG-50//GO is 2.72 Ω, much lower than that of Mn$_3$O$_4$//GO (3.95 Ω) and rGO//GO (3.88 Ω). Such distinct reduced resistance can probably be attributed to the hierarchical loosely-stacked structure of MG-50 and the synergistic effect between Mn$_3$O$_4$ nanoparticles and rGO that facilitate fast ion transportation.[22,52] The intercept of the Nyquist plot in the high frequency region is related to the bulk resistance (R_S). It is observed that the R_S value of MG-50//GO (0.72 Ω) is still smaller than those of Mn$_3$O$_4$//GO (0.84 Ω) and rGO//GO (1.06 Ω), representing the low internal resistance of the electrode materials and small ohmic resistance of the electrolyte[52] of MG-50//GO. Therefore, the low R_s and R_{CT} values are beneficial to the achievement of the high rate capability of MG-

50//GO. All the electrochemical results show the good capacitive performance of the MG composite, which may promote its application in the energy storage field.

4. Conclusions

In summary, we present a facile and low-cost solution-phase method to synthesize a Mn$_3$O$_4$/rGO (MG) composite electrode material by assembling Mn$_3$O$_4$ nanoparticles with high uniformity and fine granularity on rGO nanosheets. Moreover, the quantity of Mn$_3$O$_4$ nanoparticles can be easily controlled by regulating the weight ratio of Mn$_3$O$_4$ to rGO. Interestingly, the morphology of Mn$_3$O$_4$ is changed by introducing rGO into the fabrication system. The optimal reducing conditions were finally determined from the XRD patterns. Electrochemical characteristics show that the obtained MG composite exhibits a good electrochemical performance with high specific capacitance, large energy density and excellent long-term cycling stability. Thus, Mn$_3$O$_4$/rGO composites are promising electrode materials for energy storage applications.

Conflicts of interest

There are no conflicts to declare.

Acknowledgements

References

1 P. Yang, Y. Ding, Z. Lin, Z. Chen, Y. Li, P. Qiang, M. Ebrahimi, W. Mai, C. P. Wong and Z. L. Wang, Low-Cost High-Performance Solid-State Asymmetric Supercapacitors Based on MnO$_2$ Nanowires and Fe$_2$O$_3$ Nanotubes, *Nano Lett.*, 2014, **14**, 731–736.

2 T. Y. Wei, X. L. Wei, Y. Gao and H. M. Li, Large Scale Production of Biomass-Derived Nitrogen-Doped Porous Carbon Materials for Supercapacitors, *Electrochim. Acta*, 2015, **169**, 186–194.

3 S. S. Delekta, A. D. Smith, J. Li and M. Östling, Inkjet Printed Highly Transparent and Flexible Graphene Micro-Supercapacitors, *Nanoscale*, 2017, **9**, 6998–7005.

4 X. Tian, S. Zhu, J. Peng, Y. Zuo, G. Wang, X. Guo, N. Zhao, Y. Ma and L. Ma, Synthesis of Micro-and Meso-Porous Carbon Derived from Cellulose as an Electrode Material for Supercapacitors, *Electrochim. Acta*, 2017, **241**, 170–178.

5 F. Gao, J. Qu, Z. Zhao, Q. Zhou, B. Li and J. Qiu, A Green Strategy for the Synthesis of Graphene Supported Mn$_3$O$_4$ Nanocomposites from Graphitized Coal and Their Supercapacitor Application, *Carbon*, 2014, **80**, 640–650.

6 X. Yang, J. Yu, Z. Lin and R. Fu, Investigation on the Applicable Pore Size of Nanoporous Carbon for
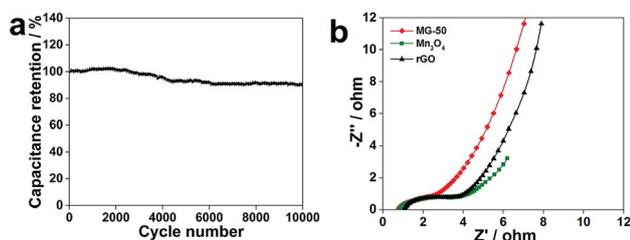
Fig. 7 (a) Cycling performance of MG-50//GO at the current density of 8 A g^{-1} over 10 000 cycles. (b) EIS of the three different supercapacitor cells.

Electrochemical Double-Layer Formation at Different Current Densities, *Electrochim. Acta*, 2017, **241**, 189–196.

7 D.-Y. Lee, G.-H. An and H.-J. Ahn, High-Surface-Area Tofu Based Activated Porous Carbon for Electrical Double-Layer Capacitors, *J. Ind. Eng. Chem.*, 2017, **52**, 121–127.

8 D. Chen, D. Ding, X. Li, G. H. Waller, X. Xiong, M. A. El-Sayed and M. Liu, Probing the Charge Storage Mechanism of a Pseudocapacitive MnO_2 Electrode Using in Operando Raman Spectroscopy, *Chem. Mater.*, 2015, **27**, 6608–6619.

9 S. Mondal, U. Rana and S. Malik, Graphene Quantum Dot-Doped Polyaniline Nanofiber as High Performance Supercapacitor Electrode Materials, *Chem. Commun.*, 2015, **51**, 12365–12368.

10 L. Bao, J. Zang and X. Li, Flexible Zn_2SnO_4/MnO_2 Core/Shell Nanocable-Carbon Microfiber Hybrid Composites for High-Performance Supercapacitor Electrodes, *Nano Lett.*, 2011, **11**, 1215–1220.

11 C. Liu, H. Song, C. Zhang, Y. Liu, C. Zhang, X. Nan and G. Cao, Coherent Mn_3O_4-Carbon Nanocomposites with Enhanced Energy-Storage Capacitance, *Nano Res.*, 2015, **8**, 3372–3383.

12 P. Simon and Y. Gogotsi, Materials for Electrochemical Capacitors, *Nat. Mater.*, 2008, **7**, 845–854.

13 X. Tian, H. Ma, Z. Li, S. Yan, L. Ma, F. Yu, G. Wang, X. Guo, Y. Ma and C. Wong, Flute Type Micropores Activated Carbon from Cotton Stalk for High Performance Supercapacitors, *J. Power Sources*, 2017, **359**, 88–96.

14 J. H. Bang, H.-M. Lee, K.-H. An and B.-J. Kim, A Study on Optimal Pore Development of Modified Commercial Activated Carbons for Electrode Materials of Supercapacitors, *Appl. Surf. Sci.*, 2017, **415**, 61–66.

15 M. Vujković, L. Matović, J. Krstić, M. Stojmenović, A. Đukić, B. Babić and S. Mentus, Mechanically Activated Carbonized Rayon Fibers as an Electrochemical Supercapacitor in Aqueous Solutions, *Electrochim. Acta*, 2017, **245**, 796–806.

16 Z. Bo, W. Zhu, W. Ma, Z. Wen, X. Shuai, J. Chen, J. Yan, Z. Wang, K. Cen and X. Feng, Vertically Oriented Graphene Bridging Active-Layer/Current-Collector Interface for Ultrahigh Rate Supercapacitors, *Adv. Mater.*, 2013, **25**, 5799–5806.

17 V. Vinoth, J. J. Wu, A. M. Asiri, T. Lana-Villarreal, P. Bonete and S. Anandan, SnO_2-Decorated Multiwalled Carbon Nanotubes and Vulcan Carbon through a Sonochemical Approach for Supercapacitor Applications, *Ultrason. Sonochem.*, 2016, **29**, 205–212.

18 Y. Chen, M. Han, Y. Tang, J. Bao, S. Li, Y. Lan and Z. Dai, Polypyrrole-Polyoxometalate/Reduced Graphene Oxide Ternary Nanohybrids for Flexible, All-Solid-State Supercapacitors, *Chem. Commun.*, 2015, **51**, 12377–12380.

19 A. Inamdar, Y. Jo, J. Kim, J. Han, S. Pawar, R. Kalubarme, C. Park, J. Hong, Y. Park and W. Jung, Synthesis and Enhanced Electrochemical Supercapacitive Properties of Manganese Oxide Nanoflake Electrodes, *Energy*, 2015, **83**, 532–538.

20 B. G. S. Raj, R. N. R. Ramprasad, A. M. Asiri, J. J. Wu and S. Anandan, Ultrasound Assisted Synthesis of Mn_3O_4 Nanoparticles Anchored Graphene Nanosheets for Supercapacitor Applications, *Electrochim. Acta*, 2015, **156**, 127–137.

21 B. Wang, J. Park, C. Wang, H. Ahn and G. Wang, Mn_3O_4 Nanoparticles Embedded into Graphene Nanosheets: Preparation, Characterization, and Electrochemical Properties for Supercapacitors, *Electrochim. Acta*, 2010, **55**, 6812–6817.

22 G. Cheng, T. Kou, J. Zhang, C. Si, H. Gao and Z. Zhang, O_2^{2-}/O^- Functionalized Oxygen-Deficient Co_3O_4 Nanorods as High Performance Supercapacitor Electrodes and Electrocatalysts towards Water Splitting, *Nano Energy*, 2017, **38**, 155–166.

23 M. Zhang, Y. Wang, D. Pan, Y. Li, Z. Yan and J. Xie, Nitrogen-doped 3D Graphene/MWNTs Nano-Frameworks Embedded Co_3O_4 for High Electrochemical Performance Supercapacitors, *ACS Sustainable Chem. Eng.*, 2017, **5**, 5099–5107.

24 M. Yu, Y. Han, J. Li and L. Wang, One-Step Synthesis of Sodium Carboxymethyl Cellulose-Derived Carbon Aerogel/Nickel Oxide Composites for Energy Storage, *Chem. Eng. J.*, 2017, **324**, 287–295.

25 B. Rezaei, A. R. T. Jahrom and A. A. Ensafi, $Co(OH)_2$ Nanoparticles Deposited on Reduced Graphene Oxide Nanoflake as a Suitable Electrode Material for Supercapacitor and Oxygen Evolution Reaction in Alkaline Media, *Int. J. Hydrogen Energy*, 2017, **42**, 16538–16546.

26 A. Khaleed, A. Bello, J. Dangbegnon, M. Madito, O. Olaniyan, F. Barzegar, K. Makgopa, K. Oyedotun, B. Mwakikunga and S. Ray, Solvothermal Synthesis of Surfactant Free Spherical Nickel Hydroxide/Graphene Oxide Composite for Supercapacitor Application, *J. Alloys Compd.*, 2017, **721**, 80–91.

27 L. Wang, Z. H. Dong, Z. G. Wang, F. X. Zhang and J. Jin, Layered α-$Co(OH)_2$ Nanocones as Electrode Materials for Pseudocapacitors: Understanding the Effect of Interlayer Space on Electrochemical Activity, *Adv. Funct. Mater.*, 2013, **23**, 2758–2764.

28 C.-L. Liu, K.-H. Chang, C.-C. Hu and W.-C. Wen, Microwave-Assisted Hydrothermal Synthesis of Mn_3O_4/Reduced Graphene Oxide Composites for High Power Supercapacitors, *J. Power Sources*, 2012, **217**, 184–192.

29 G. Jin, X. Xiao, S. Li, K. Zhao, Y. Wu, D. Sun and F. Wang, Strongly Coupled Graphene/Mn_3O_4 Composite with Enhanced Electrochemical Performance for Supercapacitor Electrode, *Electrochim. Acta*, 2015, **178**, 689–698.

30 K. Anilkumar, M. Manoj, B. Jinisha, V. Pradeep and S. Jayalekshmi, Mn_3O_4/reduced Graphene Oxide Nanocomposite Electrodes with Tailored Morphology for High Power Supercapacitor Applications, *Electrochim. Acta*, 2017, **236**, 424–433.

31 L. Li, K. H. Seng, H. Liu, I. P. Nevirkovets and Z. Guo, Synthesis of Mn_3O_4-Anchored Graphene Sheet Nanocomposites via a Facile, Fast Microwave Hydrothermal Method and Their Supercapacitive Behavior, *Electrochim. Acta*, 2013, **87**, 801–808.

32 J. Xu, X. Fan, Q. Xia, Z. Shao, B. Pei, Z. Yang, Z. Chen and W. Zhang, A Highly Atom-Efficient Strategy to Synthesize

Reduced Graphene Oxide-Mn_3O_4 Nanoparticles Composites for Supercapacitors, *J. Alloys Compd.*, 2016, **685**, 949–956.

33 Y. Xu, H. Bai, G. Lu, C. Li and G. Shi, Flexible Graphene Films *via* the Filtration of Water-Soluble Noncovalent Functionalized Graphene Sheets, *J. Am. Chem. Soc.*, 2008, **130**, 5856–5857.

34 A. Alabadi, S. Razzaque, Z. Dong, W. Wang and B. Tan, Graphene Oxide-Polythiophene Derivative Hybrid Nanosheet for Enhancing Performance of Supercapacitor, *J. Power Sources*, 2016, **306**, 241–247.

35 Y. Li, J. Qu, F. Gao, S. Lv, L. Shi, C. He and J. Sun, Situ Fabrication of Mn_3O_4 Decorated Graphene Oxide as a Synergistic Catalyst for Degradation of Methylene Blue, *Appl. Catal., B*, 2015, **162**, 268–274.

36 P. Rosaiah, J. Zhu, D. P. Shaik, O. Hussain, Y. Qiu and L. Zhao, Reduced Graphene Oxide/Mn_3O_4 Nanocomposite Electrodes with Enhanced Electrochemical Performance for Energy Storage Applications, *J. Electroanal. Chem.*, 2017, **794**, 78–85.

37 K. Ai, Y. Liu, L. Lu, X. Cheng and L. Huo, A Novel Strategy for Making Soluble Reduced Graphene Oxide Sheets Cheaply by Adopting an Endogenous Reducing Agent, *J. Mater. Chem.*, 2011, **21**, 3365–3370.

38 L. T. Ye, Z. S. Li, X. F. Zhang, F. L. Lei and S. Lin, One-Step Microwave Synthesis of Pt (Pd)/Cu_2O/GNs Composites and Their Electro-Photosynergistic Catalytic Properties for Methanol Oxidation, *J. Mater. Chem. A*, 2014, **2**, 21010–21019.

39 Y. Song, R. Zhao, K. Zhang, J. Ding, X. Lv, M. Chen and J. Xie, Facile Synthesis of Mn_3O_4/Double-Walled Carbon Nanotube Nanocomposites and Its Excellent Supercapacitive Behavior, *Electrochim. Acta*, 2017, **230**, 350–357.

40 Y. Wu, S. Liu, H. Wang, X. Wang, X. Zhang and G. Jin, A Novel Solvothermal Synthesis of Mn_3O_4/Graphene Composites for Supercapacitors, *Electrochim. Acta*, 2013, **90**, 210–218.

41 H. Chai, J. Xu, J. Han, Y. Su, Z. Sun, D. Jia and W. Zhou, Facile Synthesis of Mn_3O_4-rGO Hybrid Materials for the High-Performance Electrocatalytic Reduction of Oxygen, *J. Colloid Interface Sci.*, 2017, **488**, 251–257.

42 M. Toupin, T. Brousse and D. Bélanger, Charge Storage Mechanism of MnO_2 Electrode Used in Aqueous Electrochemical Capacitor, *Chem. Mater.*, 2004, **16**, 3184–3190.

43 S. Wu, X. Wu, G. Wang, L. Li, K. Tang, K. Huang, S. Feng, X. Dong, Z. Liu and B. Zhao, High-Yield Preparation of K-Birnessite Layered Nanoflake, *Electrochim. Acta*, 2016, **218**, 66–73.

44 J. W. Lee, A. S. Hall, J.-D. Kim and T. E. Mallouk, A Facile and Template-Free Hydrothermal Synthesis of Mn_3O_4 Nanorods on Graphene Sheets for Supercapacitor Electrodes with Long Cycle Stability, *Chem. Mater.*, 2012, **24**, 1158–1164.

45 K. Makgopa, K. Raju, P. M. Ejikeme and K. I. Ozoemena, High-Performance Mn_3O_4/Onion-Like Carbon (OLC) Nanohybrid Pseudocapacitor: Unravelling the Intrinsic Properties of OLC Against Other Carbon Supports, *Carbon*, 2017, **117**, 20–32.

46 Y. Zhang, L. Si, B. Zhou, B. Zhao, Y. Zhu, L. Zhu and X. Jiang, Synthesis of Novel Graphene Oxide/Pristine Graphene/Polyaniline Ternary Composites and Application to Supercapacitor, *Chem. Eng. J.*, 2016, **288**, 689–700.

47 H. Gao, F. Xiao, C. B. Ching and H. Duan, Flexible All-Solid-State Asymmetric Supercapacitors Based on Free-Standing Carbon Nanotube/Graphene and Mn_3O_4 Nanoparticle/Graphene Paper Electrodes, *ACS Appl. Mater. Interfaces*, 2012, **4**, 7020–7026.

48 C. Zhang, L. Wang, Y. Zhao, Y. Tian and J. Liang, Self-Assembly Synthesis of Graphene Oxide Double-Shell Hollow-Spheres Decorated with Mn_3O_4 for Electrochemical Supercapacitors, *Carbon*, 2016, **107**, 100–108.

49 Y. Wang, Z. Ji, X. Shen, K. Xu and A. Yuan, Facile Synthesis of Mn_3O_4/Reduced Graphene Oxide Nanocomposites with Enhanced Capacitive Performance, *J. Alloys Compd.*, 2016, **684**, 366–371.

50 R. Rajagopal, Y. S. Lee and K.-S. Ryu, Synthesis and Electrochemical Analysis of Nb_2O_5-TiO_2/H-rGO Sandwich Type Layered Architecture Electrode for Supercapacitor Application, *Chem. Eng. J.*, 2017, **325**, 611–623.

51 B. Saravanakumar, K. K. Purushothaman and G. Muralidharan, Interconnected V_2O_5 Nanoporous Network for High-Performance Supercapacitors, *ACS Appl. Mater. Interfaces*, 2012, **4**, 4484–4490.

52 Y. Ge, C. Wang, K. Shu, C. Zhao, X. Jia, S. Gambhir and G. G. Wallace, A Facile Approach for Fabrication of Mechanically Strong Graphene/Polypyrrole Films with Large Areal Capacitance for Supercapacitor Applications, *RSC Adv.*, 2015, **5**, 102643–102651.